Variational Monte Carlo Study of the 1/9-Magnetization Plateau in Kagome Antiferromagnets

Li-Wei He,[1] Shun-Li Yu,[1,2,*] and Jian-Xin Li[1,2,†]

[1]*National Laboratory of Solid State Microstructures and Department of Physics, Nanjing University, Nanjing 210093, China*

[2]*Collaborative Innovation Center of Advanced Microstructures, Nanjing University, Nanjing 210093, China*

(Received 29 February 2024; revised 7 June 2024; accepted 29 July 2024; published 30 August 2024)

Motivated by very recent experimental observations of the 1/9-magnetization plateaus in $YCu_3(OH)_{6+x}Br_{3-x}$ and $YCu_3(OD)_{6+x}Br_{3-x}$, our study delves into the magnetic-field-induced phase transitions in the nearest-neighbor antiferromagnetic Heisenberg model on the kagome lattice using the variational Monte Carlo technique. We uncover a phase transition from a zero-field Dirac spin liquid to a field-induced magnetically disordered phase that exhibits the 1/9-magnetization plateau. Through a comprehensive analysis encompassing the magnetization distribution, spin correlations, chiral order parameter, topological entanglement entropy, ground-state degeneracy, Chern number, and excitation spectrum, we pinpoint the phase associated with this magnetization plateau as a chiral $\mathbb{Z}_3$ topological quantum spin liquid and elucidate its diverse physical properties.

DOI: 10.1103/PhysRevLett.133.096501

The kagome lattice is an exceptional platform for exploring novel many-body states [1–55], owing to its distinctive lattice and electron structures. In particular, the spin-1/2 kagome antiferromagnet with only the nearest-neighbor Heisenberg exchange interactions has attracted significant interest as a promising candidate for realizing the quantum spin liquid (QSL). Although many theoretical studies have suggested that the ground state of this system is likely a QSL [17–31], there remains a lack of consensus regarding the precise nature of this QSL state. On the experimental front, the kagome antiferromagnets like herbertsmithite [34–37], Zn-barlowite [38–42], and $YCu_3(OH)_{6+x}Br_{3-x}$ [43,44] have shown great promise as QSL materials. Moreover, when subjected to an external magnetic field, the spin-1/2 kagome antiferromagnet can also manifest novel quantum states [45–55], further highlighting its potential as an ideal platform for exploring exotic quantum states of matter.

Very recently, it was reported experimentally that 1/9-magnetization plateaus were observed in $YCu_3(OH)_{6+x}Br_{3-x}$ and $YCu_3(OD)_{6+x}Br_{3-x}$ [56–58]. In contrast to the commonly observed 1/3-magnetization plateaus characterized by classical spin orders in other frustrated antiferromagnets with triangular and honeycomb lattices [59–67], this 1/9-plateau phase is a magnetically disordered state. This suggests that the mechanism underlying this phase is fundamentally distinct from the order-by-disorder mechanism that typically gives rise to the 1/3-magnetization plateaus. However, experimental consensus on certain fundamental characteristics of this phase, such as its gapped or gapless nature, still remains elusive. Theoretically, despite several numerical studies on the spin-1/2 kagome antiferromagnetic Heisenberg model having corroborated the existence of the 1/9-magnetization plateau [49,51,55], its precise nature remains a subject of debate. The density matrix renormalization group (DMRG) calculation has proposed that this plateau phase may correspond to a $\mathbb{Z}_3$ spin liquid [49], whereas the tensor network methods have provided evidence supporting a valence bond solid (VBS) interpretation [51,55]. Given these divergent perspectives, more comprehensive investigations employing a variety of methodologies are necessary to unravel this exotic magnetic phenomenon.

In this Letter, we investigate the effect of an external magnetic field on the kagome antiferromagnetic Heisenberg model using the variational Monte Carlo (VMC) method. Without a field, our results reveal that the ground state is a Dirac spin liquid (DSL). This DSL is robust against weak fields; however, as the field increases beyond a threshold, a new disordered state emerges. This state has a nonzero chiral order parameter and triples the primitive cell. Its magnetization directly jumps onto $M/M_s = 1/9$ (M_s the saturation magnetization) and remains constant over a wide range of field. In this 1/9-plateau phase, the magnetization distribution is uniform. The topological entanglement entropy (TEE) is approximately $\gamma = 1.05$, which is very close to $\ln 3 \approx 1.1$ within numerical error. Based on the relation $\gamma = \ln D \approx \ln 3$, where D is the total quantum dimension, we refer to this exotic state as a chiral $\mathbb{Z}_3$ topological QSL. Moreover, the ground-state degeneracy (GSD) is 9, implying that this state has an Abelian topological order ($D^2 = 9$).

*Contact author: slyu@nju.edu.cn

†Contact author: jxli@nju.edu.cn

We further unveil the characteristic spin excitation spectrum of this $\mathbb{Z}_3$ QSL, providing key signatures to identify it directly in experiments.

The kagome antiferromagnetic Heisenberg model in an external magnetic field is written as

$$H = J\sum_{\langle ij\rangle} \boldsymbol{S}_i \cdot \boldsymbol{S}_j - B_z \sum_i S_i^z, \tag{1}$$

where $\langle ij\rangle$ signifies the sum over nearest-neighbor bonds, $\boldsymbol{S}_i$ represents the spin-1/2 operator at site i (S_i^z its z component), J is the exchange interaction, and B_z the magnitude of the magnetic field.

Following the standard VMC framework, we introduce a fermionic representation for spin operators [68–71], i.e., $\boldsymbol{S}_i = \frac{1}{2}\psi_i^\dagger \boldsymbol{\sigma} \psi_i$ with $\psi_i = (c_{i,\uparrow}, c_{i,\downarrow})^T$, which adhere to the local constraint $\psi_i^\dagger \psi_i = 1$. We then decouple the model (1) into a quadratic mean-field Hamiltonian [72],

$$H_{\mathrm{mf}} = \sum_{\langle ij\rangle} (t_{ij}\psi_i^\dagger \psi_j + \mathrm{H.c}) - \sum_i \mu \psi_i^\dagger \sigma^z \psi_i, \tag{2}$$

where t_{ij} represents the spinon hopping and μ is the chemical potential that is tuned by the magnetic field. Our analysis of various possible states with spinon pairings reveals that such states are not energetically favorable [72], so the mean-field (mf) Hamiltonian considered does not include spinon pairing terms. We construct the variational wave function as $|\Psi(p)\rangle = P_G|GS\rangle_{\mathrm{mf}}$ with $p = (t_{ij}, \mu)$ embodying the variational parameters, P_G representing the Gutzwiller projector that imposes the strict single-occupation constraint, and $|GS\rangle_{\mathrm{mf}}$ the ground state of H_{mf}. The optimization of p is achieved through the minimization of the energy $E(p) = \langle\Psi(p)|H|\Psi(p)\rangle/\langle\Psi(p)|\Psi(p)\rangle$, utilizing the stochastic reconfiguration method [73,74]. For our main results, we utilize lattice sizes of $N = 16 \times 12 \times 3$ for the DSL and $N = 12 \times 12 \times 3$ for the $\mathbb{Z}_3$ QSL and VBS states [72], respectively, unless specified otherwise.

In the regime of low magnetic fields, our VMC calculations reveal that the ground state is a gapless DSL. This state is characterized within the framework of mean-field Hamiltonian (2) by uniform spinon hopping amplitudes, accompanied by an alternating flux pattern of 0 and π through the triangular and hexagonal plaquettes, as depicted in Fig. 1(a). As illustrated in Fig. 1(c), the mean-field spinon dispersion exhibits characteristic Dirac cones. This DSL is consistent with the results obtained in previous theoretical researches [17,21,23,24,27]. Owing to the vanishing zero-energy density of states for the spinons, the magnetic field must reach a threshold to produce a noticeable magnetization response, as shown in Fig. 2(b). The false plateau with $M/M_s < 0.01$ in Fig. 2(b) is caused by the finite-size effect, it asymptotically approaches to zero with increasing system size [72].

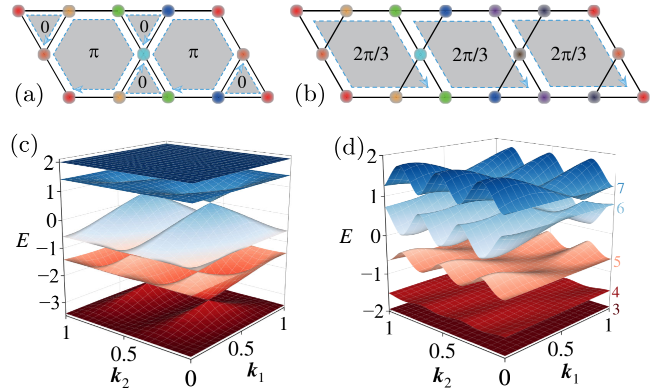

FIG. 1. Mean-field *Ansätze* and spinon band structures. The mean-field *Ansätze* for the DSL (a) and $\mathbb{Z}_3$ QSL (b), with flux pattern represented by shaded areas, arrows, and corresponding values. (c) Complete mean-field spinon band structure for the DSL. (d) Selected mean-field spinon bands (bands 3 to 7) for the $\mathbb{Z}_3$ QSL, using optimal variational parameters derived from VMC calculations at $B_z/J = 0.5$.

When the field B_z exceeds $0.35J$, the DSL is no longer energetically favorable, as shown in Fig. 2(a). The identified phase transition point is in quantitative agreement with that derived from the previous DMRG and tensor network methods [49,51,55]. However, there was a significant divergence in previous studies regarding the nature of the phase after the phase transition, as discussed above. Our VMC calculations reveal that the ground state for $0.35 \lesssim B_z/J \lesssim 0.63$ is a $\mathbb{Z}_3$ QSL, whose nature will be discussed in detail subsequently. In the process to search for the most energetically favored state, we have carried out a comprehensive examination of a variety of gauge-inequivalent

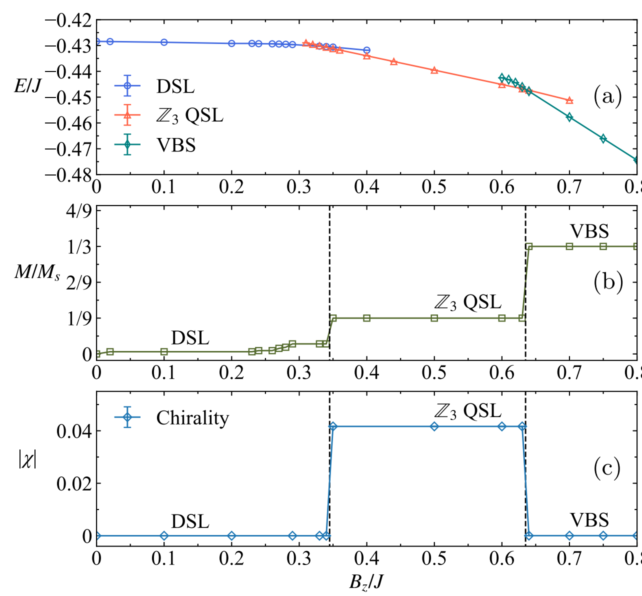

FIG. 2. Variational energy E (a), average magnetization M/M_s (b), and chiral order parameter $|\chi|$ (c) as functions of B_z.

Ansätze, including the uniform resonating-valence-bond state, DSL, chiral spin liquid, $\mathbb{Z}_2$ QSLs with different spinon pairings, $\mathbb{Z}_3$ QSL, and several VBS states [72]. For the $\mathbb{Z}_3$ QSL and VBS states, we extended the unit cell to encompass nine sites, equivalent to three primitive cells of the kagome lattice. For the $\mathbb{Z}_3$ QSL, the amplitudes of the parameter t_{ij} in the mean-field Hamiltonian (2) and the fluxes within each primitive cell are uniform, making the 3×1 and $\sqrt{3} \times \sqrt{3}$ extended unit cells equivalent. Our calculations utilize the 3×1 extended unit cell, which facilitates setting the flux in each primitive cell to be $2\pi/3$, as depicted in Fig. 1(b). To optimize the phases of the parameter $t_{ij} = te^{i\theta_{ij}}$, we incorporate 15 independent θ_{ij} into our set of variational parameters for the sake of generality. Given that the VBS states can break the translational and rotational symmetries, both the 3×1 and $\sqrt{3} \times \sqrt{3}$ extended unit cells are used for the VBS states.

The ground-state energy curve depicted in Fig. 2(a) clearly shows two phase transitions: one from DSL to $\mathbb{Z}_3$ QSL at $B_z/J \approx 0.35$, the other from $\mathbb{Z}_3$ QSL to a $\sqrt{3} \times \sqrt{3}$ VBS [72] at $B_z/J \approx 0.63$. In Fig. 2(b), the magnetization ratio M/M_s of the field-induced $\mathbb{Z}_3$ QSL for $0.35 \lesssim B_z/J \lesssim 0.63$ is observed to stabilize at 1/9. This forms a robust magnetization plateau, which aligns with the experimental findings in compounds $\mathrm{YCu_3(OH)_{6+x}Br_{3-x}}$ and $\mathrm{YCu_3(OD)_{6+x}Br_{3-x}}$ [56–58]. From the perspective of spinons, the first five of the nine available spinon bands [see Fig. 1(d)] are occupied by spin-up spinons, while spin-down spinons occupy only the first four, resulting in a magnetization ratio of $M/M_s = (N_\uparrow - N_\downarrow)/N = 1/9$. We also notice that the $\sqrt{3} \times \sqrt{3}$ VBS for $B_z/J > 0.63$ exhibits a 1/3-magnetization plateau, consistent with the experimental observations [56,57]. Furthermore, we calculate the chiral order parameter defined as $|\chi| = |\sum_{i \in \triangle/\triangledown} \boldsymbol{S}_{i1} \cdot (\boldsymbol{S}_{i2} \times \boldsymbol{S}_{i3})|/N_{\triangle/\triangledown}$ [75,76], where the indices 1, 2, and 3 correspond to vertexes (arranged clockwise) in an elementary triangle i, and $N_{\triangle/\triangledown}$ represents the total number of triangles. As depicted in Fig. 2(c), $|\chi|$ is found to be nonzero and constant throughout the 1/9-plateau phase, while it is zero in the DSL and $\sqrt{3} \times \sqrt{3}$ VBS phases. In the magnetization process, the only nonzero chirality of this $\mathbb{Z}_3$ QSL can be detected experimentally using polarized neutron scattering [77].

We then examine the distribution of magnetization across the lattice for the 1/9-magnetization plateau phase. As shown in Fig. 3(a), the magnetization M/M_s at each site is very close to 1/9. Such uniformity is in stark contrast to the behavior seen in the magnetization plateau phases of other frustrated antiferromagnets [59–67], which typically exhibit a nonuniform magnetization within their expanded unit cells. On the other hand, though the magnetic moment distribution superficially resembles that of conventional ferromagnetic states, the underlying spin-spin correlations are profoundly different. As depicted in Fig. 3(b), the equal-time spatial spin-spin correlation function $C(r)$ in this phase exhibits a rapid decay to zero with the distance between pairs of sites. This behavior differs essentially from the long-range correlations of ferromagnetic order, where spins at infinitely separated distances remain perfectly correlated. The presence of such short-range spin-spin correlations is a distinguishing characteristic of a QSL.

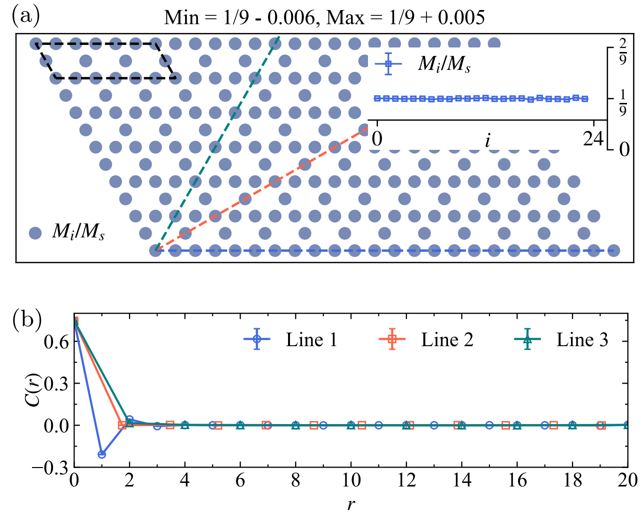

FIG. 3. (a) Distribution of magnetization M_i/M_s in the 1/9-magnetization plateau phase. The black dashed lines highlight the unit cell for this phase. The sphere diameters correspond to the magnetization magnitude at each site. Since the magnetization distribution is almost uniform, we explicitly provide the minimum and maximum values of magnetization. The magnetization values along a representative direction (indicated by the dashed blue line) are also shown in the inset. (b) Spin-spin correlation functions $C(r)$ along three representative directions, as indicated by the dashed lines with corresponding colors in (a). Here, $C(r) = \sum_{\gamma \in \{x,y,z\}} \langle \Psi | \tilde{S}^\gamma_{r_0} \tilde{S}^\gamma_{r_0 + r\delta_i} | \Psi \rangle$ with $\tilde{S}^\gamma_{\boldsymbol{r}} = S^\gamma_{\boldsymbol{r}} - \langle \Psi | S^\gamma_{\boldsymbol{r}} | \Psi \rangle$, $\boldsymbol{\delta}_i$ being the unit vectors of the three directions and r the distance.

Our subsequent analysis focuses on the topological properties of the 1/9-magnetization plateau phase. An important quantity for characterizing topological properties is the TEE [78–83]. To obtain the TEE, we partition the system into two subsystems, A and B, and calculate the Renyi entropy $S_n = (1-n)^{-1} \log[\mathrm{Tr}(\rho_A^n)]$, where $\rho_A = \mathrm{Tr}_B |\Psi\rangle\langle\Psi|$ and $|\Psi\rangle$ is the ground-state wave function [72,83]. For a short-ranged Hamiltonian, the entanglement entropy is predicted to follow $S(L) = \alpha L - \gamma$, with L representing the boundary length of a contractible patch with codimension-1 boundary. The coefficient α is n-dependent, while γ, the TEE, is independent of n. We focus on the Renyi entropy with index $n = 2$, which is more feasible to compute with our VMC method [72,83]. Moreover, this TEE can reflect the total quantum dimension D of the topological order, i.e., $\gamma = \ln D$. To extract the TEE, we calculate the entropy S_2 for varying sizes of the shaded region and apply a linear extrapolation to $L \to 0$ in order to eliminate the area-law-associated αL term.

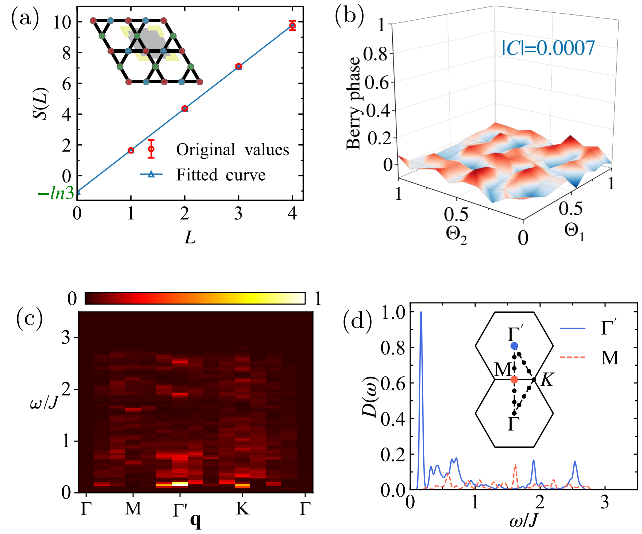

FIG. 4. (a) Entanglement entropy of the 1/9-magnetization plateau phase as a function of subsystem size. We choose the shape of the subsystem as a diamond, as indicated by the shaded area in the inset. The horizontal axis means that the area of the subsystem is L^2 times of primitive cell. The best fit to $S(L) = \alpha L - \gamma$ gives $\gamma \sim 1.05$. (b) Distribution of Berry phase in the Θ_1-Θ_2 space, which is discretized into a grid of 100 plaquettes. The Berry phase over each small plaquette is approximately proportional to the Berry curvature. (c) Spin excitation spectrum for a lattice size of $6 \times 6 \times 3$. (d) Energy distribution curves of the spectra at Γ' and M. The insert shows the momentum path Γ-M-Γ'-K-Γ used in (c).

As shown in Fig. 4(a), the TEE of the 1/9-magnetization plateau phase is $\gamma \approx 1.05 \approx \ln 3$, suggesting that the total quantum dimension D should be 3. Therefore, we can infer that this disordered phase with 1/9 magnetization is a $\mathbb{Z}_3$ QSL.

The nontrivial topological nature of this chiral $\mathbb{Z}_3$ QSL can be further characterized by its GSD [84–86]. We have constructed nine projected ground states by applying different boundary conditions to the mean-field Hamiltonian H_{mf}, each corresponding to varying magnetic fluxes threading the two hole of the torus lattice [72]. These states are denoted as $|\Psi_{\alpha,\beta}\rangle = P_G|GS_{\alpha,\beta}\rangle_{\mathrm{mf}}$, where the fluxes α and β take on the values of $2n\pi/3$ with $n \in \{0, 1, 2\}$. The ground-state degeneracy aligns with the linear independence of these nine variational wave functions. To elucidate this degeneracy, we computed the overlaps between each pair of the nine states, assembling an overlap matrix [72,87,88]. Analysis of this matrix revealed that all nine of its eigenvalues are nonzero, confirming that the GSD is $n_g = 9$, as summarized in Table I. Given that the total quantum dimension is $D^2 = 9$, it shows that this chiral $\mathbb{Z}_3$ QSL manifests an Abelian topological order, satisfying the relation $D^2 = n_g$.

Moreover, unlike other chiral spin liquids [87–89], the chiral $\mathbb{Z}_3$ QSL discussed here has a topological Chern number of zero. As shown in Fig. 1(d), the mean-field spinon dispersion exhibits gaps between any two bands, thereby the Chern number of each band is well-defined (see Table II). From the perspective of spinons, the Chern number arising from the spin-up spinons is $C_\uparrow = \sum_{i=1}^{5} C_i = -1$ for the magnetization ratio $M/M_s = 1/9$, while the spin-down spinons yield a Chern number $C_\downarrow = \sum_{i=1}^{4} C_i = 1$. Thus, the total Chern number is zero, but the spin Chern number $C_s = (C_\uparrow - C_\downarrow)/2$ is nonzero, which is similar to that of quantum spin Hall states [90]. To verify the zero Chern number beyond the mean-field level, we construct the projective many-body wave functions with twisted boundary condition: $c_{i+L_j,\uparrow} = c_{i,\uparrow}e^{i\Theta_j}$ and $c_{i+L_j,\downarrow} = c_{i,\downarrow}e^{-i\Theta_j}$, with $j = 1, 2$ indicating the two primitive lattice vector directions, L_j the lattice size along the j direction, and $\Theta_j \in [0, 2\pi]$ the twisted boundary phase. The Chern number is calculated by integrating the Berry curvature $\mathcal{F}(\Theta_1, \Theta_2)$ [72,87,91]: $C = (1/2\pi)\int_0^{2\pi} d\Theta_1 \int_0^{2\pi} d\Theta_2 \mathcal{F}(\Theta_1, \Theta_2)$. As depicted in Fig. 4(b), the Berry curvature has both positive and negative values, resulting in a net Chern number of zero. This zero Chern number also implies a zero chiral central charge [92]. Considering its long-range entanglement and the GSD of $n_g = 9$, we can identify this $\mathbb{Z}_3$ QSL as a topologically ordered phase with a rank 9 topological order, denoted as 9_0^B in Ref. [92]. Moreover, the nonzero chirality of this $\mathbb{Z}_3$ QSL is also consistent with the existence of two 9_0^B states that break time-reversal symmetry and are mutual time-reversed states.

Finally, we discuss how to experimentally identify the $\mathbb{Z}_3$ QSL by measuring the spin excitation spectrum. Figure 4(c) shows the longitudinal dynamic structure factor $D(\boldsymbol{q}, \omega)$ [72] calculated using the VMC method [29,93,94]. The excitation spectrum is gapped and manifests as a broad continuum, originating from the fractionalization of the $S = 1$ spin excitations. A notable feature is the enhanced periodicity of its lower edge, as evidenced by the presence of multiple minima with the same energy in the first

TABLE I. Eigenvalues of the 9×9 overlap matrix with the elements $\mathcal{O}_{\alpha\beta;\alpha'\beta'} = \langle\Psi_{\alpha,\beta}|\Psi_{\alpha',\beta'}\rangle$ for the $\mathbb{Z}_3$ QSL, calculated with lattice size $N = 12 \times 12 \times 3 = 432$.

ε_1	ε_2	ε_3	ε_4	ε_5	ε_6	ε_7	ε_8	ε_9
3.547	0.916	0.901	0.875	0.837	0.825	0.809	0.146	0.144

TABLE II. Chern numbers C of the mean-field spinon bands for the $\mathbb{Z}_3$ QSL.

Index	1	2	3	4	5	6	7	8	9
C	1	−2	1	1	−2	4	−2	−2	1

Brillouin zone. This is related to the translation symmetry fractionalization [95,96], and the unique fractionalization characteristics of the $\mathbb{Z}_3$ QSL can be used to distinguish it from other QSL states [29,94]. Additionally, the ω dependence of the spectra at specific momenta can also serve as a basis for experimental identification of the $\mathbb{Z}_3$ QSL. As shown in Fig. 4(d), the spectra at Γ' and M exhibit several characteristic peaks, and they differ significantly from the spectra of other QSL states in the kagome system [29,94].

In summary, motivated by experimental observations of the 1/9-magnetization plateaus in $YCu_3(OH)_{6+x}Br_{3-x}$ and $YCu_3(OD)_{6+x}Br_{3-x}$, we utilize the VMC method to investigate the magnetization of the antiferromagnetic Heisenberg model on the kagome lattice, with a particular emphasis on elucidating the nature of the 1/9-magnetization plateau. By increasing the magnetic field, we observe a field-induced magnetically disordered phase exhibiting a 1/9-magnetization plateau. Detailed investigations of the magnetization pattern, spin correlations, chiral order parameter, and topological entanglement entropy have led us to identify this 1/9-magnetization plateau phase as a chiral $\mathbb{Z}_3$ topological QSL. We also highlight key features in the spin excitation spectrum that can be used for the experimental identification of this $\mathbb{Z}_3$ QSL. It should be noted, however, that our model does not include disorder effects, which are unavoidable in real materials. The influence of disorder effects on the magnetization plateau phase is also an important issue that warrants further study.

Acknowledgments—We thank Q.-H. Wang, Z.-X. Liu, and Z.-L. Gu for help discussions. This work was supported by National Key Projects for Research and Development of China (Grant No. 2021YFA1400400) and the National Natural Science Foundation of China (No. 92165205, No. 12074175, No. 12374137, and No. 12434005).

[1] P. W. Leung and V. Elser, Numerical studies of a 36-site kagomé antiferromagnet, Phys. Rev. B **47**, 5459 (1993).
[2] M. B. Hastings, Dirac structure, RVB, and Goldstone modes in the kagomé antiferromagnet, Phys. Rev. B **63**, 014413 (2000).
[3] S. V. Isakov, S. Wessel, R. G. Melko, K. Sengupta, and Y. B. Kim, Hard-core bosons on the kagome lattice: Valence-bond solids and their quantum melting, Phys. Rev. Lett. **97**, 147202 (2006).
[4] W.-H. Ko, P. A. Lee, and X.-G. Wen, Doped kagome system as exotic superconductor, Phys. Rev. B **79**, 214502 (2009).
[5] A. O'Brien, F. Pollmann, and P. Fulde, Strongly correlated fermions on a kagome lattice, Phys. Rev. B **81**, 235115 (2010).
[6] E. Tang, J.-W. Mei, and X.-G. Wen, High-temperature fractional quantum Hall states, Phys. Rev. Lett. **106**, 236802 (2011).
[7] A. Rüegg and G. A. Fiete, Fractionally charged topological point defects on the kagome lattice, Phys. Rev. B **83**, 165118 (2011).
[8] S.-L. Yu and J.-X. Li, Chiral superconducting phase and chiral spin-density-wave phase in a Hubbard model on the kagome lattice, Phys. Rev. B **85**, 144402 (2012).
[9] J.-X. Yin *et al.*, Giant and anisotropic many-body spin–orbit tunability in a strongly correlated kagome magnet, Nature (London) **562**, 91 (2018).
[10] L. Ye, M. Kang, J. Liu, F. Von Cube, C. R. Wicker, T. Suzuki, C. Jozwiak, A. Bostwick, E. Rotenberg, D. C. Bell, L. Fu, R. Comin, and J. G. Checkelsky, Massive Dirac fermions in a ferromagnetic kagome metal, Nature (London) **555**, 638 (2018).
[11] D. F. Liu, A. J. Liang, E. K. Liu, Q. N. Xu, Y. W. Li, C. Chen, D. Pei, W. J. Shi, S. K. Mo, P. Dudin, T. Kim, C. Cacho, G. Li, Y. Sun, L. X. Yang, Z. K. Liu, S. S. P. Parkin, C. Felser, and Y. L. Chen, Magnetic Weyl semimetal phase in a Kagomé crystal, Science **365**, 1282 (2019).
[12] B. R. Ortiz, S. M. L. Teicher, Y. Hu, J. L. Zuo, P. M. Sarte, E. C. Schueller, A. M. Milinda Abeykoon, M. J. Krogstad, S. Rosenkranz, R. Osborn, R. Seshadri, L. Balents, J. He, and S. D. Wilson, CsV_3Sb_5: A $\mathbb{Z}_2$ topological kagome metal with a superconducting ground state, Phys. Rev. Lett. **125**, 247002 (2020).
[13] H. Chen *et al.*, Roton pair density wave in a strong-coupling kagome superconductor, Nature (London) **599**, 222 (2021).
[14] L. Nie *et al.*, Charge-density-wave-driven electronic nematicity in a kagome superconductor, Nature (London) **604**, 59 (2022).
[15] L. Zheng, Z. Wu, Y. Yang, L. Nie, M. Shan, K. Sun, D. Song, F. Yu, J. Li, D. Zhao, S. Li, B. Kang, Y. Zhou, K. Liu, Z. Xiang, J. Ying, Z. Wang, T. Wu, and X. Chen, Emergent charge order in pressurized kagome superconductor CsV_3Sb_5, Nature (London) **611**, 682 (2022).
[16] J.-X. Yin, B. Lian, and M. Z. Hasan, Topological kagome magnets and superconductors, Nature (London) **612**, 647 (2022).
[17] Y. Ran, M. Hermele, P. A. Lee, and X.-G. Wen, Projected-wave-function study of the spin-1/2 Heisenberg model on the kagomé lattice, Phys. Rev. Lett. **98**, 117205 (2007).
[18] H. C. Jiang, Z. Y. Weng, and D. N. Sheng, Density matrix renormalization group numerical study of the kagome antiferromagnet, Phys. Rev. Lett. **101**, 117203 (2008).
[19] S. Yan, D. A. Huse, and S. R. White, Spin-liquid ground state of the $S = 1/2$ kagome Heisenberg antiferromagnet, Science **332**, 1173 (2011).
[20] S. Depenbrock, I. P. McCulloch, and U. Schollwöck, Nature of the spin-liquid ground state of the $S = 1/2$ Heisenberg model on the kagome lattice, Phys. Rev. Lett. **109**, 067201 (2012).
[21] Y. Iqbal, F. Becca, S. Sorella, and D. Poilblanc, Gapless spin-liquid phase in the kagome spin-$\frac{1}{2}$ Heisenberg antiferromagnet, Phys. Rev. B **87**, 060405(R) (2013).
[22] Y. Iqbal, D. Poilblanc, and F. Becca, Spin-$\frac{1}{2}$ Heisenberg $J_1 - J_2$ antiferromagnet on the kagome lattice, Phys. Rev. B **91**, 020402(R) (2015).
[23] H. J. Liao, Z. Y. Xie, J. Chen, Z. Y. Liu, H. D. Xie, R. Z. Huang, B. Normand, and T. Xiang, Gapless spin-liquid ground state in the $S = 1/2$ kagome antiferromagnet, Phys. Rev. Lett. **118**, 137202 (2017).

[24] Y.-C. He, M. P. Zaletel, M. Oshikawa, and F. Pollmann, Signatures of Dirac cones in a DMRG study of the kagome Heisenberg model, Phys. Rev. X **7**, 031020 (2017).

[25] J.-W. Mei, J.-Y. Chen, H. He, and X.-G. Wen, Gapped spin liquid with $\mathbb{Z}_2$ topological order for the kagome Heisenberg model, Phys. Rev. B **95**, 235107 (2017).

[26] X. Chen, S.-J. Ran, T. Liu, C. Peng, Y.-Z. Huang, and G. Su, Thermodynamics of spin-1/2 Kagomé Heisenberg antiferromagnet: Algebraic paramagnetic liquid and finite-temperature phase diagram, Sci. Bull. **63**, 1545 (2018).

[27] W. Zhu, X. Chen, Y.-C. He, and W. Witczak-Krempa, Entanglement signatures of emergent Dirac fermions: Kagome spin liquid and quantum criticality, Sci. Adv. **4**, eaat5535 (2018).

[28] A. M. Läuchli, J. Sudan, and R. Moessner, $S=\frac{1}{2}$ kagome Heisenberg antiferromagnet revisited, Phys. Rev. B **100**, 155142 (2019).

[29] C. Zhang and T. Li, Variational study of the ground state and spin dynamics of the spin-$\frac{1}{2}$ kagome antiferromagnetic Heisenberg model and its implication for herbertsmithite $ZnCu_3(OH)_6Cl_2$, Phys. Rev. B **102**, 195106 (2020).

[30] B. Bernu, L. Pierre, K. Essafi, and L. Messio, Effect of perturbations on the kagome $S=\frac{1}{2}$ antiferromagnet at all temperatures, Phys. Rev. B **101**, 140403(R) (2020).

[31] N. Astrakhantsev, F. Ferrari, N. Niggemann, T. Müller, A. Chauhan, A. Kshetrimayum, P. Ghosh, N. Regnault, R. Thomale, J. Reuther, T. Neupert, and Y. Iqbal, Pinwheel valence bond crystal ground state of the spin-$\frac{1}{2}$ Heisenberg antiferromagnet on the shuriken lattice, Phys. Rev. B **104**, L220408 (2021).

[32] R. R. P. Singh and D. A. Huse, Ground state of the spin-1/2 kagome-lattice Heisenberg antiferromagnet, Phys. Rev. B **76**, 180407(R) (2007).

[33] G. Evenbly and G. Vidal, Frustrated antiferromagnets with entanglement renormalization: Ground state of the spin-$\frac{1}{2}$ Heisenberg model on a kagome lattice, Phys. Rev. Lett. **104**, 187203 (2010).

[34] J. S. Helton, K. Matan, M. P. Shores, E. A. Nytko, B. M. Bartlett, Y. Yoshida, Y. Takano, A. Suslov, Y. Qiu, J.-H. Chung, D. G. Nocera, and Y. S. Lee, Spin dynamics of the spin-1/2 kagome lattice antiferromagnet $ZnCu_3(OH)_6Cl_2$, Phys. Rev. Lett. **98**, 107204 (2007).

[35] T.-H. Han, J. S. Helton, S. Chu, D. G. Nocera, J. A. Rodriguez-Rivera, C. Broholm, and Y. S. Lee, Fractionalized excitations in the spin-liquid state of a kagome-lattice antiferromagnet, Nature (London) **492**, 406 (2012).

[36] M. Fu, T. Imai, T.-H. Han, and Y. S. Lee, Evidence for a gapped spin-liquid ground state in a kagome Heisenberg antiferromagnet, Science **350**, 655 (2015).

[37] P. Khuntia, M. Velazquez, Q. Barthélemy, F. Bert, E. Kermarrec, A. Legros, B. Bernu, L. Messio, A. Zorko, and P. Mendels, Gapless ground state in the archetypal quantum kagome antiferromagnet $ZnCu_3(OH)_6Cl_2$, Nat. Phys. **16**, 469 (2020).

[38] Z. Feng, Z. Li, X. Meng, W. Yi, Y. Wei, J. Zhang, Y.-C. Wang, W. Jiang, Z. Liu, S. Li, F. Liu, J. Luo, S. Li, G. qing Zheng, Z. Y. Meng, J.-W. Mei, and Y. Shi, Gapped spin-1/2 spinon excitations in a new kagome quantum spin liquid compound $Cu_3Zn(OH)_6FBr$, Chin. Phys. Lett. **34**, 077502 (2017).

[39] Z. Feng, Y. Wei, R. Liu, D. Yan, Y.-C. Wang, J. Luo, A. Senyshyn, C. d. Cruz, W. Yi, J.-W. Mei, Z. Y. Meng, Y. Shi, and S. Li, Effect of Zn doping on the antiferromagnetism in kagome $Cu_{4-x}Zn_x(OH)_6FBr$, Phys. Rev. B **98**, 155127 (2018).

[40] Y. Wei, X. Ma, Z. Feng, D. Adroja, A. Hillier, P. Biswas, A. Senyshyn, A. Hoser, J.-W. Mei, Z. Y. Meng, H. Luo, Y. Shi, and S. Li, Magnetic phase diagram of $Cu_{4-x}Zn_x(OH)_6FBr$ studied by neutron-diffraction and μSR techniques, Chin. Phys. Lett. **37**, 107503 (2020).

[41] K. Tustain, B. Ward-O'Brien, F. Bert, T. Han, H. Luetkens, T. Lancaster, B. M. Huddart, P. J. Baker, and L. Clark, From magnetic order to quantum disorder in the Zn-barlowite series of $S=1/2$ kagomé antiferromagnets, npj Quantum Mater. **5**, 74 (2020).

[42] Y. Fu, M.-L. Lin, L. Wang, Q. Liu, L. Huang, W. Jiang, Z. Hao, C. Liu, H. Zhang, X. Shi, J. Zhang, J. Dai, D. Yu, F. Ye, P. A. Lee, P.-H. Tan, and J.-W. Mei, Dynamic fingerprint of fractionalized excitations in single-crystalline $Cu_3Zn(OH)_6FBr$, Nat. Commun. **12**, 3048 (2021).

[43] Z. Zeng, X. Ma, S. Wu, H.-F. Li, Z. Tao, X. Lu, X. H. Chen, J.-X. Mi, S.-J. Song, G.-H. Cao, G. Che, K. Li, G. Li, H. Luo, Z. Y. Meng, and S. Li, Possible Dirac quantum spin liquid in the kagome quantum antiferromagnet $YCu_3(OH)_6Br_2[Br_x(OH)_{1-x}]$, Phys. Rev. B **105**, L121109 (2022).

[44] A. Xu, B. Liu, Z. Zeng, L. Yan, and S. Li, Quantum-spin-liquid state in kagome $YCu_3(OH)_6[(Cl_xBr_{1-x})_{3-y}(OH)_y]$: The role of alternate-bond hexagons and beyond, arXiv:2311.13089.

[45] M. E. Zhitomirsky, Field-induced transitions in a kagomé antiferromagnet, Phys. Rev. Lett. **88**, 057204 (2002).

[46] M. E. Zhitomirsky and H. Tsunetsugu, Exact low-temperature behavior of a kagomé antiferromagnet at high fields, Phys. Rev. B **70**, 100403(R) (2004).

[47] H. Nakano and T. Sakai, Magnetization process of kagome-lattice Heisenberg antiferromagnet, J. Phys. Soc. Jpn. **79**, 053707 (2010).

[48] T. Sakai and H. Nakano, Critical magnetization behavior of the triangular- and kagome-lattice quantum antiferromagnets, Phys. Rev. B **83**, 100405(R) (2011).

[49] S. Nishimoto, N. Shibata, and C. Hotta, Controlling frustrated liquids and solids with an applied field in a kagome Heisenberg antiferromagnet, Nat. Commun. **4**, 2287 (2013).

[50] S. Capponi, O. Derzhko, A. Honecker, A. M. Läuchli, and J. Richter, Numerical study of magnetization plateaus in the spin-$\frac{1}{2}$ kagome Heisenberg antiferromagnet, Phys. Rev. B **88**, 144416 (2013).

[51] T. Picot, M. Ziegler, R. Orús, and D. Poilblanc, Spin-S kagome quantum antiferromagnets in a field with tensor networks, Phys. Rev. B **93**, 060407(R) (2016).

[52] X. Plat, T. Momoi, and C. Hotta, Kinetic frustration induced supersolid in the $S=\frac{1}{2}$ kagome lattice antiferromagnet in a magnetic field, Phys. Rev. B **98**, 014415 (2018).

[53] J. Schnack, J. Schulenburg, and J. Richter, Magnetism of the $N=42$ kagome lattice antiferromagnet, Phys. Rev. B **98**, 094423 (2018).

[54] R. Okuma, D. Nakamura, T. Okubo, A. Miyake, A. Matsuo, K. Kindo, M. Tokunaga, N. Kawashima, S. Takeyama, and

Z. Hiroi, A series of magnon crystals appearing under ultrahigh magnetic fields in a kagomé antiferromagnet, Nat. Commun. **10**, 1229 (2019).
[55] D. Z. Fang, N. Xi, S.-J. Ran, and G. Su, Nature of the 1/9-magnetization plateau in the spin-$\frac{1}{2}$ kagome Heisenberg antiferromagnet, Phys. Rev. B **107**, L220401 (2023).
[56] G. Zheng, Y. Zhu, K.-W. Chen, B. Kang, D. Zhang, K. Jenkins, A. Chan, Z. Zeng, A. Xu, O. A. Valenzuela, J. Blawat, J. Singleton, P. A. Lee, S. Li, and L. Li, Unconventional magnetic oscillations in kagome Mott insulators, arXiv:2310.07989.
[57] S. Suetsugu, T. Asaba, Y. Kasahara, Y. Kohsaka, K. Totsuka, B. Li, Y. Zhao, Y. Li, M. Tokunaga, and Y. Matsuda, Emergent spin-gapped magnetization plateaus in a spin-1/2 perfect kagome antiferromagnet, Phys. Rev. Lett. **132**, 226701 (2024).
[58] S. Jeon, D. Wulferding, Y. Choi, S. Lee, K. Nam, K. H. Kim, M. Lee, T.-H. Jang, J.-H. Park, S. Lee, S. Choi, C. Lee, H. Nojiri, and K.-Y. Choi, One-ninth magnetization plateau stabilized by spin entanglement in a kagome antiferromagnet, Nat. Phys. **20**, 435 (2024).
[59] T. Ono, H. Tanaka, H. Aruga Katori, F. Ishikawa, H. Mitamura, and T. Goto, Magnetization plateau in the frustrated quantum spin system Cs_2CuBr_4, Phys. Rev. B **67**, 104431 (2003).
[60] H. Tsujii, C. R. Rotundu, T. Ono, H. Tanaka, B. Andraka, K. Ingersent, and Y. Takano, Thermodynamics of the up-up-down phase of the $S = \frac{1}{2}$ triangular-lattice antiferromagnet Cs_2CuBr_4, Phys. Rev. B **76**, 060406(R) (2007).
[61] Y. Shirata, H. Tanaka, A. Matsuo, and K. Kindo, Experimental realization of a spin-1/2 triangular-lattice Heisenberg antiferromagnet, Phys. Rev. Lett. **108**, 057205 (2012).
[62] H. D. Zhou, C. Xu, A. M. Hallas, H. J. Silverstein, C. R. Wiebe, I. Umegaki, J. Q. Yan, T. P. Murphy, J.-H. Park, Y. Qiu, J. R. D. Copley, J. S. Gardner, and Y. Takano, Successive phase transitions and extended spin-excitation continuum in the $S=\frac{1}{2}$ triangular-lattice antiferromagnet $Ba_3CoSb_2\mathbf{O}_9$, Phys. Rev. Lett. **109**, 267206 (2012).
[63] J. Hwang, E. S. Choi, F. Ye, C. R. Dela Cruz, Y. Xin, H. D. Zhou, and P. Schlottmann, Successive magnetic phase transitions and multiferroicity in the spin-one triangular-lattice antiferromagnet $Ba_3NiNb_2\mathbf{O}_9$, Phys. Rev. Lett. **109**, 257205 (2012).
[64] T. Susuki, N. Kurita, T. Tanaka, H. Nojiri, A. Matsuo, K. Kindo, and H. Tanaka, Magnetization process and collective excitations in the $S=1/2$ triangular-lattice Heisenberg antiferromagnet $Ba_3CoSb_2\mathbf{O}_9$, Phys. Rev. Lett. **110**, 267201 (2013).
[65] Y. Kamiya, L. Ge, T. Hong, Y. Qiu, D. L. Quintero-Castro, Z. Lu, H. B. Cao, M. Matsuda, E. S. Choi, C. D. Batista, M. Mourigal, H. D. Zhou, and J. Ma, The nature of spin excitations in the one-third magnetization plateau phase of $Ba_3CoSb_2O_9$, Nat. Commun. **9**, 2666 (2018).
[66] T. Inami, Y. Ajiro, and T. Goto, Magnetization process of the triangular lattice antiferromagnets, $RbFe(MoO_4)_2$ and $CsFe(SO_4)_2$, J. Phys. Soc. Jpn. **65**, 2374 (1996).
[67] Y. Shangguan *et al.*, A one-third magnetization plateau phase as evidence for the Kitaev interaction in a honeycomb-lattice antiferromagnet, Nat. Phys. **19**, 1883 (2023).
[68] X.-G. Wen, Quantum orders and symmetric spin liquids, Phys. Rev. B **65**, 165113 (2002).
[69] Y.-M. Lu, Y. Ran, and P. A. Lee, $\mathbb{Z}_2$ spin liquids in the $S = \frac{1}{2}$ Heisenberg model on the kagome lattice: A projective symmetry-group study of Schwinger fermion mean-field states, Phys. Rev. B **83**, 224413 (2011).
[70] S. Bieri, C. Lhuillier, and L. Messio, Projective symmetry group classification of chiral spin liquids, Phys. Rev. B **93**, 094437 (2016).
[71] Q.-R. Zhao and Z.-X. Liu, Thermal properties and instability of a U(1) spin liquid on the triangular lattice, Phys. Rev. Lett. **127**, 127205 (2021).
[72] See Supplemental Material at http://link.aps.org/supplemental/10.1103/PhysRevLett.133.096501 for detailed information on the mean-field Hamiltonian, various variational wave functions, analysis of the finite-size effects, ground-state degeneracy, topological entanglement entropy, Chern number, and calculation schemes in VMC.
[73] S. Sorella and L. Capriotti, Green function Monte Carlo with stochastic reconfiguration: An effective remedy for the sign problem, Phys. Rev. B **61**, 2599 (2000).
[74] S. Sorella, Generalized Lanczos algorithm for variational quantum Monte Carlo, Phys. Rev. B **64**, 024512 (2001).
[75] X. G. Wen, Vacuum degeneracy of chiral spin states in compactified space, Phys. Rev. B **40**, 7387 (1989).
[76] A. Wietek, A. Sterdyniak, and A. M. Läuchli, Nature of chiral spin liquids on the kagome lattice, Phys. Rev. B **92**, 125122 (2015).
[77] W. Schweika, M. Valldor, J. D. Reim, and U. K. Rößler, Chiral spin liquid ground state in $YBaCo_3FeO_7$, Phys. Rev. X **12**, 021029 (2022).
[78] M. Levin and X.-G. Wen, Detecting topological order in a ground state wave function, Phys. Rev. Lett. **96**, 110405 (2006).
[79] A. Kitaev and J. Preskill, Topological entanglement entropy, Phys. Rev. Lett. **96**, 110404 (2006).
[80] M. B. Hastings, I. González, A. B. Kallin, and R. G. Melko, Measuring Renyi entanglement entropy in quantum Monte Carlo simulations, Phys. Rev. Lett. **104**, 157201 (2010).
[81] Y. Zhang, T. Grover, and A. Vishwanath, Entanglement entropy of critical spin liquids, Phys. Rev. Lett. **107**, 067202 (2011).
[82] H.-C. Jiang, Z. Wang, and L. Balents, Identifying topological order by entanglement entropy, Nat. Phys. **8**, 902 (2012).
[83] Y. Zhang, T. Grover, and A. Vishwanath, Topological entanglement entropy of $\mathbb{Z}_2$ spin liquids and lattice Laughlin states, Phys. Rev. B **84**, 075128 (2011).
[84] X. G. Wen, Vacuum degeneracy of chiral spin states in compactified space, Phys. Rev. B **40**, 7387 (1989).
[85] X. G. Wen and Q. Niu, Ground-state degeneracy of the fractional quantum Hall states in the presence of a random potential and on high-genus Riemann surfaces, Phys. Rev. B **41**, 9377 (1990).
[86] A. Y. Kitaev, Fault-tolerant quantum computation by anyons, Ann. Phys. (Amsterdam) **303**, 2 (2003).

[87] W.-J. Hu, W. Zhu, Y. Zhang, S. Gong, F. Becca, and D. N. Sheng, Variational Monte Carlo study of a chiral spin liquid in the extended Heisenberg model on the kagome lattice, Phys. Rev. B **91**, 041124(R) (2015).

[88] W.-J. Hu, S.-S. Gong, and D. N. Sheng, Variational Monte Carlo study of chiral spin liquid in quantum antiferromagnet on the triangular lattice, Phys. Rev. B **94**, 075131 (2016).

[89] F. D. M. Haldane and D. P. Arovas, Quantized spin currents in two-dimensional chiral magnets, Phys. Rev. B **52**, 4223 (1995).

[90] D. N. Sheng, Z. Y. Weng, L. Sheng, and F. D. M. Haldane, Quantum spin-Hall effect and topologically invariant Chern numbers, Phys. Rev. Lett. **97**, 036808 (2006).

[91] Q. Niu, D. J. Thouless, and Y.-S. Wu, Quantized Hall conductance as a topological invariant, Phys. Rev. B **31**, 3372 (1985).

[92] X.-G. Wen, A theory of $2+1$D bosonic topological orders, Natl. Sci. Rev. **3**, 68 (2015).

[93] F. Ferrari, A. Parola, S. Sorella, and F. Becca, Dynamical structure factor of the $J_1 - J_2$ Heisenberg model in one dimension: The variational Monte Carlo approach, Phys. Rev. B **97**, 235103 (2018).

[94] F. Ferrari, S. Niu, J. Hasik, Y. Iqbal, D. Poilblanc, and F. Becca, Static and dynamical signatures of Dzyaloshinskii-Moriya interactions in the Heisenberg model on the kagome lattice, SciPost Phys. **14**, 139 (2023).

[95] A. M. Essin and M. Hermele, Classifying fractionalization: Symmetry classification of gapped $\mathbb{Z}_2$ spin liquids in two dimensions, Phys. Rev. B **87**, 104406 (2013).

[96] Y. Qi and M. Cheng, Classification of symmetry fractionalization in gapped $\mathbb{Z}_2$ spin liquids, Phys. Rev. B **97**, 115138 (2018).